Design of a Polarization Rotating SIW-Based Reflector for Polarimetric Radar Application

Tim Freialdenhoven, Thomas Bertuch, *Member, IEEE*, Stephan Stanko, Denis Nötel, Diana I. L. Vorst, and Thomas Dallmann, *Member, IEEE*

***Abstract*— Polarimetric radar systems are beneficial to identifying and classifying targets but require multiple transmit or receive channels with different polarizations. This leads to a high hardware effort and thus higher costs. To use a single, linear polarized radar sensor as a polarimetric system, a frequency-dependent, polarization rotating reflector which can be placed in front of the radar antenna is presented. The reflector is based on a frequency selective surface (FSS) consisting of slot-excited substrate integrated waveguide (SIW) resonators. Resonator modes are analyzed and an equivalent circuit diagram to describe the filter functionality is developed. For using the described FSS as reflective structure, the design focuses on 45° oblique incidence. Different field vectors for normal and oblique incident angles are considered and different cavity modes for these cases are analyzed. An undesired mode is suppressed by an additional plated through via hole and slot impedances are matched. Reflector designs for normal and oblique incident angles are presented for 15 GHz (*Ku*-band) and afterward adapted to 35 GHz (*Ka*-band). The frequency band of operation with 12% fractional bandwidth is divided into two 4.5% subbands which allows a frequency-dependent polarization rotation of a linear polarized electromagnetic wave. Investigations on the fabrication accuracies are presented and reflectors for both bands are manufactured. Measurements are performed with a vector network analyzer and results fit well to the simulated curves. In the band of polarization rotation reflection, the matching is better than −13 dB and dielectric losses of less than 1 dB are achieved.**

***Index Terms*— Frequency selective surface (FSS), polarization rotating surface, radar polarimetry, reflector, resonator, substrate-integrated waveguide (SIW).**

I. Introduction

RADAR systems are multidimensional measurement devices that are capable of reliably measuring distances, angles velocities, or scattering parameters. The demands on radars are constantly increasing nowadays. Examples are the need for higher resolutions, improved efficiencies, lower false alarm rates, and smaller sensor dimensions in applications like autonomous driving, security, space surveillance, defense, meteorology, or geology. For conventional radar systems, it is difficult to deal with heterogeneous scenes and to correctly identify and classify targets. Through the use of polarimetric radar systems, additional information can be gained by measuring the polarimetric scattering matrix [1]. Therefore, the radar sensor has to transmit and receive multiple polarizations that are affected differently by the observed scene.

When scattering matrix coefficients are available, an appropriate target decomposition algorithm can be utilized to separate different scattering mechanisms and, as a result, improved target characterization can be carried out. Moreover, this allows for example to distinguish single reflections from double reflections [1].

Polarimetric systems are used in countless meteorological or geological applications, e.g., for weather recording, surface characterization, ground topography estimation, sea ice, or iceberg observation. Airborne or satellite-borne polarimetric synthetic aperture radar (SAR) systems are used for data acquisition, where the data can then be processed depending on the application [2]–[6]. In the automotive domain, road users and vehicle types must be correctly identified, which can be done more reliably by analyzing the scattering signature considering also polarization information. Therefore, especially for autonomous driving, polarimetric radars have become more attractive in the recent years [7], [8].

Polarimetric scattering information can only be extracted by a radar system with hardware that transmits and receives multiple polarizations. Commonly multiple channels with different polarizations for transmitter (TX) and receiver (RX) are used. Due to high costs, large sensor dimensions, more power consumption, and an increased probability of failure, this approach is rarely applicable, especially for mass-production. A promising approach to overcome these disadvantages is the use of passive, polarization selective structures which are placed in front of a nonpolarimetric radar antenna. Frequency-dependent, periodically arranged resonant structures implemented on printed circuit boards (PCBs) can be used to rotate the polarization of an incident linear polarized wave and have been presented in the previous works. In this context, "rotation" means that the electric field vector is rotated or reoriented by a static, resonant structure, changing the polarization of an impinging electromagnetic wave.

A polarization rotating reflector using resonant L-shaped slots and a rectangular substrate integrated waveguide (SIW)

Manuscript received September 24, 2019; revised January 10, 2020; accepted May 18, 2020. Date of publication June 16, 2020; date of current version October 29, 2020. *(Corresponding author: Tim Freialdenhoven.)*

Tim Freialdenhoven and Thomas Dallmann are with the Research Group Aachen, Fraunhofer Institute for High Frequency Physics and Radar Techniques FHR, 52074 Aachen, Germany (e-mail: tim.freialdenhoven@fhr.fraunhofer.de).

Thomas Bertuch is with AEM, Fraunhofer Institute for High Frequency Physics and Radar Techniques FHR, 53343 Wachtberg, Germany.

Stephan Stanko, Denis Nötel, and Diana I. L. Vorst are with HRA, Fraunhofer Institute for High Frequency Physics and Radar Techniques FHR, 53343 Wachtberg, Germany.

Color versions of one or more of the figures in this article are available online at https://ieeexplore.ieee.org.

Digital Object Identifier 10.1109/TAP.2020.3001430

cavity is proposed in [9]. This structure can also be used for oblique incidence offering a fractional bandwidth of around 3%. In contrast to reflective structures, transmissive surfaces are also practicable in which the incident wave passes through the structure, thus could be mounted straight in front of a sensor. Structures based on circular or rectangular SIW cavities excited with different slot shapes are shown in [10]–[12] for Ka-band. An approach implementing a frequency selective surface with V-shaped slots on a PCB without cavities has been proposed in [13] for 10 GHz. These structures turn a linear polarized incident electromagnetic wave up to 90° in a certain frequency band, but do not allow the incident wave to propagate without polarization rotation in a neighbored band.

The use of the proposed reflector with the characteristic to rotate the incident linear polarization with a rotation angle that depends on the frequency band and to use it for a polarimetric radar has been patented by the Fraunhofer Institute for High Frequency Physics and Radar Techniques (FHR), Wachtberg, Germany, and will be presented in this article [14].

As a first step, the working principle, frequency bands, and design concept for the frequency selective surface (FSS) are clarified in Section II. Section III considers normal and oblique incident waves, analyzes resonant modes within the SIW cavity, and introduces an equivalent circuit diagram (ECD). Moreover, designs and simulated scattering (S) parameters for different incidence angles of a plane wave are proposed for the Ku-band. Afterward, the structure is scaled to Ka-band and manufacturing tolerances are considered by using a Monte Carlo approach in Section IV. For evaluating simulation results with measurements, Section V proposes a measurement setup with vector network analyzer. S-parameter measurements of the fabricated Ku- and Ka-band reflectors are presented and discussed in Section VI. Finally, Section VII provides a summary of the work carried out.

II. Concept

The polarization rotating reflector is based on an array arrangement of identical unit cells that provide a frequency selective and polarization rotating functionality. To use the presented structure as reflector, a 45° oblique direction of incidence with respect to the surface normal direction of an electromagnetic wave is required.

Depending on the frequency of operation, the incident linear polarization is either reflected with the same polarization or converted to its orthogonal polarization according to Fig. 1(a) and (b), respectively. Therefore, the entire design bandwidth must be divided into two subbands with different reflection properties. In addition, an unusable transition band is unavoidable due to finite filter slope.

For using the presented polarization rotating reflector with an existing conventional radar system exhibiting a given operation frequency, the FSS is developed for the frequency bands given in Table I.

The reflector is implemented on a PCB with substrate material suitable for high frequencies. This approach facilitates simple and cost-effective mass production. Inspired by the promising results in [9]–[12], each unit cell consists of an SIW resonator for the purpose of rotating the polarization of the incident wave. The resonator is excited and loaded through linear polarized, orthogonal slots which can be considered as complementary dipole antennas with exchanged electric and magnetic field components according to Babinet's principle [15]. Within the rectangular SIW cavity, several modes are resonant which have to be analyzed and controlled. For the purpose of converting electromagnetic energy between both slots, a coupling element is required. Two chamfered edges integrated into the SIW cavity cause diagonal-oriented discontinuities which lead to diagonal cavity modes allowing polarization rotation.

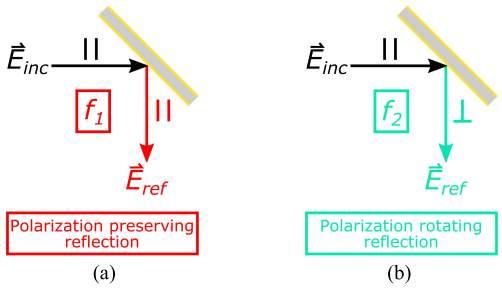

Fig. 1. Working principle of the frequency-dependent, polarization rotating reflector. (a) Polarization preserving reflection at frequency f_1. (b) Polarization rotating reflection at frequency f_2.

TABLE I
Frequency Allocation

Band	Functionality	Frequency (GHz)	Bandwidth (GHz)
Ku	Polarization preserved	14.100 – 14.865	0.765
Ku	Not used	14.865 – 15.135	0.270
Ku	Polarization rotated	15.135 – 15.900	0.765
Ka	Polarization preserved	32.900 – 34.580	1.680
Ka	Not used	34.580 – 35.420	0.840
Ka	Polarization rotated	35.420 – 37.100	1.680

For the construction of the total reflector, multiple unit cells can be combined to establish a two-dimensional, uniformly spaced, planar array. The reflector size or the number of unit cells can be selected depending on the radiation characteristic of the radar sensor used or the spacing between radar and reflector in such a way that a compromise between spillover and aperture efficiency is achieved. Fig. 2(a) shows the unit cell cross section and Fig. 2(b) depicts a two layer FSS with 2×2 unit cells consisting of SIW cavities with slanted via hole edges including crossed slots.

The reflector can be interpreted as a transceiver that receives a signal, modifies it (in this case by performing frequency filtering), and retransmits it with a certain polarization. For receiving and afterward transmitting the electromagnetic wave, a slot antenna array is used. From array theory, it is well-known that for avoidance of grating lobes, the distance between two neighboring unit cells has to be less than $(\lambda_{FS}^{min}/2)$, where λ_{FS}^{min} is the free-space wavelength at the highest frequency [15]. Due to the conductive surface at the rear side of the reflector, the slot radiation pattern deviates from the

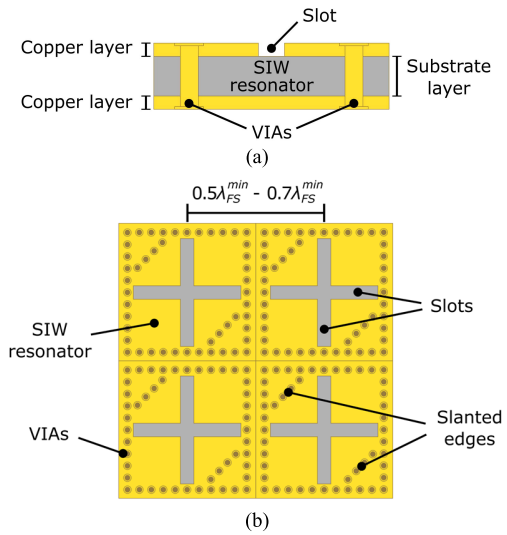

Fig. 2. Polarization rotating reflector implemented on a PCB. (a) Unit cell cross section. (b) Two layer FSS with SIW cavities and slanted edges including crossed slots.

omnidirectional dipole characteristic. The slot characteristic has a main lobe with high directivity along normal direction of the reflector surface and low directivity in perpendicular directions. Consequently, grating lobes are attenuated by the single element pattern and a slightly larger unit cell spacing is acceptable. As a result, an inter unit cell distance of $0.5\lambda_{FS}^{min} - 0.7\lambda_{FS}^{min}$ is applied.

For understanding the concept of the reflection mechanism, when the polarization is effectively rotated, the induction theorem [16] provides an instructive interpretation. For that purpose and considering plane waves only, the total field in presence of the twist reflector can be divided into an incident and a scattered field. One possible choice for the incident field consists of the incident and reflected plane waves in presence of a uniform planar metal sheet (please note the usage of the terms "field" and "wave"). Incident and reflected waves of this incident field have the same polarization. With this choice for the incident field, the scattered field is caused by perforating the metal sheet with the periodic grid of crossed slots backed by the SIW resonators. These slot/resonator combinations cause a scattered field that again consists of two contributions. One contribution cancels the co-polarized reflected wave of the incident field and the other contribution is a wave that propagates in the same direction as the reflected wave of the incident field but has an orthogonal polarization.

III. Theory and Design

Two different cases for the incidence of a planar electromagnetic wave are considered for designing the FSS. If the reflector is oriented in a Cartesian coordinate system, field components are different in normal or oblique incidence according to Fig. 3. The direction of incidence and reflection is labeled $\vec{k}_i$ and $\vec{k}_r$, respectively. In Fig. 3(a), normal incidence with $\vec{k}_i$ parallel to $\vec{n}$ is depicted, where $\vec{n}$ is the normal vector of the FSS. An impinging electromagnetic field with electric

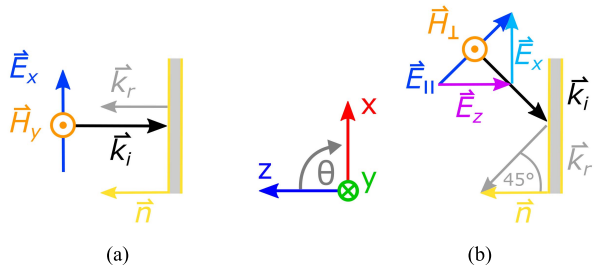

Fig. 3. Electric and magnetic fields in a reflector coordinate system. (a) Normal incidence ($\varphi = 0°, \theta = 0°$). (b) Oblique incidence ($\varphi = 0°$, $\theta = 45°$).

field vector $\vec{E}_x$ is depicted which is aligned with the x-axis of the Cartesian coordinate axis.

If the incidence is oblique which means

$$(\varphi = 0°, \theta \neq 0°) \tag{1}$$

the impinging electric field vector is no longer aligned with the coordinate axis. If the plane of incidence is spanned by $\vec{k}_i$ and $\vec{n}$, the impinging field quantities can be named parallel ($\parallel$) or perpendicular ($\perp$). Fig. 3(b) shows electric field vector $\vec{E}_\parallel$ that is compounded of x- and z-components and can be described as

$$\vec{E}_\parallel = \vec{E}_x + \vec{E}_z. \tag{2}$$

As a result, compared with normal incidence, the impinging wave couples additional field components into the SIW cavity which lead to unwanted effects that will be described in Section III-B. Thus, in a first step, normal incidence will be discussed, before the more complex case of oblique incidence is addressed.

A. Normal Incidence

For an incident electromagnetic wave that is propagating and polarized according to Fig. 3(a), an SIW cavity is modeled in CST Microwave Studio for Ku-band. As lateral simulation boundaries, the unit cell condition with periodic arrangement of unit cells is selected. From the previously mentioned array theory, the outer dimensions of a unit cell are limited to approx. $(\lambda_{FS}^{min}/2)$. To integrate slots within the SIW unit cell, a sufficiently high permittivity is required, resulting in $(\lambda_e^{cen}/2)$ slot length, where λ_e^{cen} is the effective wavelength at air–substrate interface at center frequency. Rogers RO3003 with relative permittivity $\varepsilon_r = 3$ is used for the first prototype in the Ku-band due to its excellent high-frequency performance in terms of losses. An initial substrate thickness of 1.52 mm is used to create a sufficiently thick cavity. For the understanding of the SIW cavity behavior, fields are analyzed with the Eigenmode solver of CST. For rectangular cavity resonators, mode frequencies can be easily estimated by using permittivity, geometrical dimensions, and mode order. However, since the cavity has a more complex shape and fields are influenced significantly by the top layer slots, mode resonant frequencies have been calculated numerically with CST Microwave Studio.

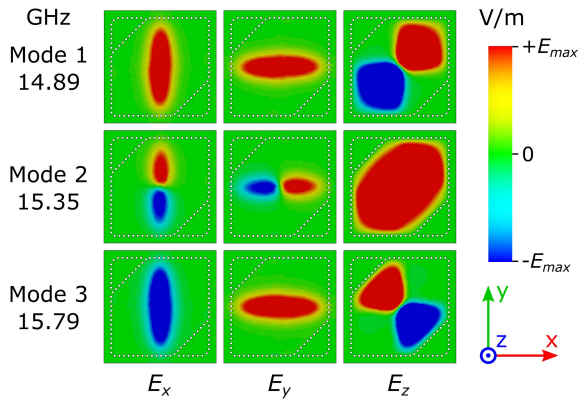

Fig. 4. Contour plots of electric field components in the SIW cavity calculated with the Eigenmode solver. Fields are depicted in a cutting xy plane and amplitudes are linearly color-coded between $\pm E_{max}$.

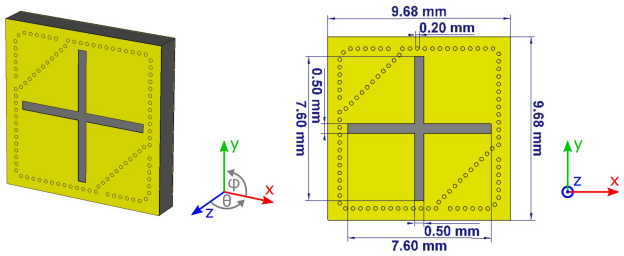

Fig. 5. CST model of Ku-band unit cell for normal incidence ($\varphi = 0°$, $\theta = 0°$) from positive z-direction.

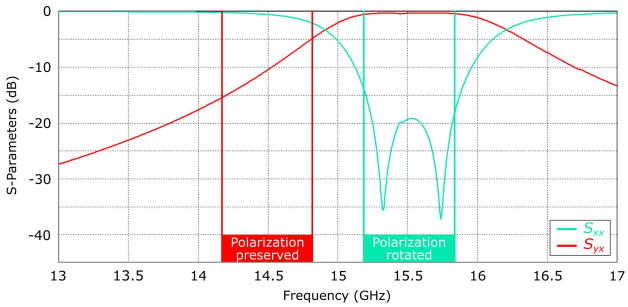

Fig. 6. Magnitude plot of S-parameters of Ku-band unit cell over frequency for normal incidence ($\varphi = 0°, \theta = 0°$) from positive z-direction.

Within the frequency band of polarization rotation according to Table I, three modes 1, 2, and 3 are resonant at 14.89, 15.35, and 15.79 GHz, respectively, depicted by field components E_x, E_y, and E_z in Fig. 4. The real part of electric field components is color-coded with a linear scale and plotted over an xy plane located at the center of the substrate material. For those modes, it can be observed that E_x and E_y components are mainly present in the slot areas. In contrast, the E_z component is strong within a diagonally oriented area within the cavity due to slanted via edges. It is obvious that a $(\lambda_e/2)$ field distribution is expected to be present along the slots for E_x and E_y, which is the case for modes 1 and 3. Mode 2 seems to consist of field components with λ_e distribution along the slots in x- and y-directions which cannot be generated by a single straight slot due to geometrical dimensions. If E_x and E_y components of mode 2 are overlaid, it can be determined that the expected $(\lambda_e/2)$ field distribution is given over two 90° folded slots with $(\lambda_e/4)$ fields occurring in the x- and y-directions. As a result, the excitation of this mode takes place as a combination of E_x and E_y over both slots. Thus, mode 2 cannot be excited by a wave impinging along normal direction. Consequently, only modes 1 and 3 are used for energy conversion between both slots. The diagonal distribution of the E_z field component is essential for the polarization rotating effect forced by slanted via edges.

The simulation model of the Ku-band reflector is depicted in Fig. 5. The upper boundary of the simulation volume is covered by the so-called Floquet port with two perpendicularly polarized Floquet modes enabled. Mode 1 is x-polarized (x) and mode 2 is perpendicular (y) polarized referring to Fig. 3(a). Both modes are transverse electromagnetic modes (TEMs) and Floquet mode 1 is excited for the simulations. The structure has been tuned in a way that slot width, slot length, and slanted via edges are suitable to achieve the desired performance and to obtain a bandpass behavior. The resulting S-parameters S_{xx} and S_{yx} given in Fig. 6 describe the reflection coefficient of Floquet mode 1 and the transmission from Floquet mode 1 to Floquet mode 2, respectively. In the lower band (14.100–14.865 GHz), a polarization preserving reflection of Floquet mode 1 occurs, showing cross polarization attenuation from 2.5 up to 15.2 dB. Especially at the upper band edge, the polarization decoupling is low which is an undesired behavior. According to the frequency allocation in Table I, the allowed unused band is required to be narrow. Therefore, the spacing between polarization preserved and rotating band is relatively small. Responsible for this is the limited filter order of the presented single layer unit cell, resulting in a weak performance at the band edges. In the upper polarization rotating band (15.135–15.900 GHz), matching of 13.1 dB up to more than 35 dB is achieved. Two resonances are present resulting in energy transfer from Floquet mode 1 to Floquet mode 2. The coupling of those resonances is dependent on how far the diagonal via edges extend into the cavity, where slight shifts of about 25 μm lead to significant changes in performance. Three different locations have been simulated, and resulting S-parameters are depicted in Fig. 7 with highlighted diagonal via edges.

The designed reflector shows a bandpass filter characteristic and consequently can be modeled by an ECD. The two orthogonal slots can be represented as parallel resonator circuits, which have low impedance far from the resonance frequency and thus allow reflections in the polarization preserving band. A high impedance state is present at resonant frequency, which ensures the undamped propagation of the signal. Both slots are coupled by an SIW cavity with chamfered edges that are crucial for polarization rotation. To emulate this function, a serial blind element is integrated resulting in the bandpass filter of fifth order depicted in Fig. 8. If the ECD is analyzed by an even–odd mode decomposition, the serial blind element must exhibit inductive behavior to obtain the same response as the unit cell. For performing an even–odd

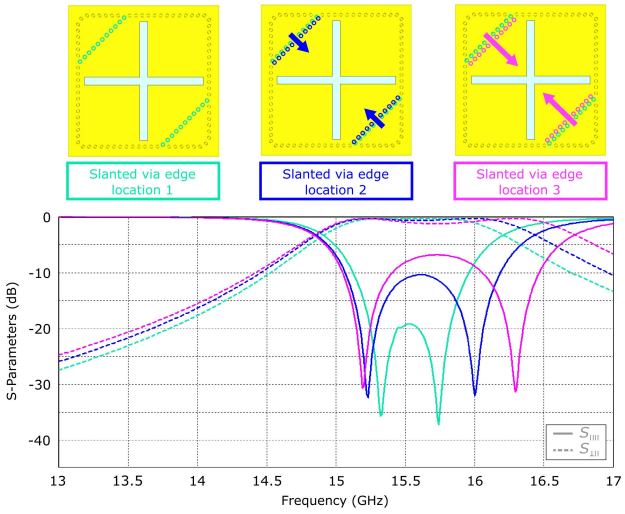

Fig. 7. Magnitude plot of S-parameters of Ku-band unit cell over frequency for normal incidence ($\varphi = 0°, \theta = 0°$) from positive z-direction for different slanted via edge locations 1, 2, and 3.

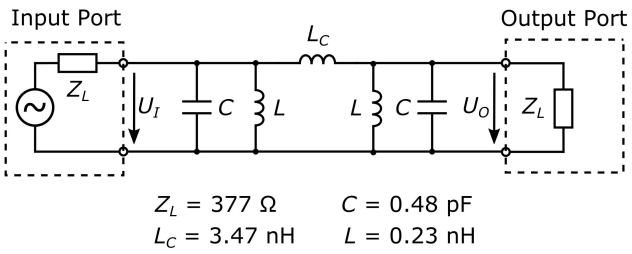

Fig. 8. ECD describing the unit cell bandpass filter characteristic.

mode decomposition, $U_I = U_O$ is applied for even mode and $U_I = -U_O$ is applied for odd mode [17]. As a result, a simplification of the circuit diagram can be done and even and odd mode resonant frequencies

$$f_{r,e} = \frac{1}{2\pi\sqrt{LC}} \tag{3}$$

$$f_{r,o} = \frac{1}{2\pi}\sqrt{\frac{L + \frac{1}{2}L_C}{LC\frac{1}{2}L_C}} \tag{4}$$

can be calculated. The change of the serial coupling inductance L_C has a similar effect on the upper resonance frequency as the change of the slanted via edges in Fig. 7.

To simulate the ECD, an input port with voltage source and 377 Ω reference impedance is used, where the port resistance corresponds to the free space characteristic impedance. An output port with 377 Ω load impedance is integrated into the model, as the system should be matched to radiate all the energy through the orthogonal slot back into the free space. Fitting the ECD filter response to the magnitude and phase of the S-parameter S_{yx} in Fig. 6 leads to the element values listed in Fig. 8. Those capacitance and inductance values can be taken to calculate the corresponding even and odd mode frequencies with (3) and (4) resulting in $f_{r,e} = 15.15$ GHz and $f_{r,o} = 16.12$ GHz. These frequencies are close to the resonant frequencies of mode 1 and mode 3 taken from Fig. 4.

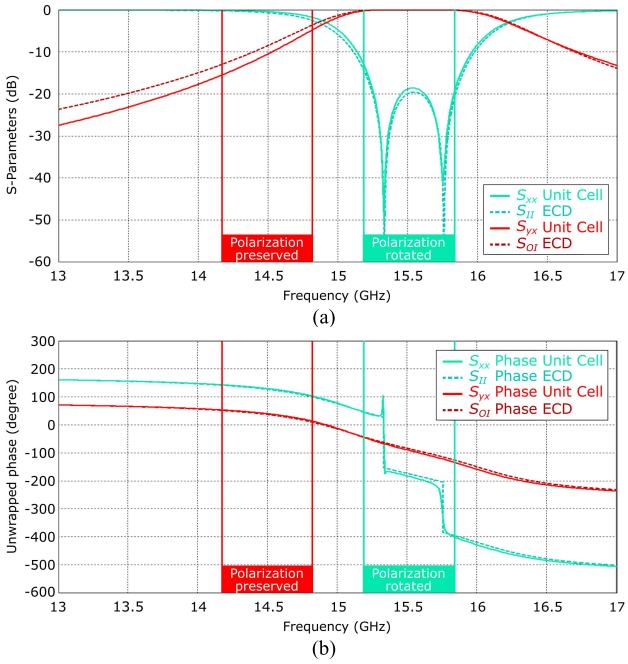

Fig. 9. S-parameters of ECD and Ku-band unit cell over frequency for normal incidence ($\varphi = 0°, \theta = 0°$) from positive z-direction. (a) Magnitude plots. (b) Phase plots.

The circuit diagram is simulated with CST Circuit & Systems Schematic and the S-parameter S_{II} and S_{OI} are obtained, where S_{II} is the reflection coefficient at the input port and S_{OI} is the transmission coefficient from input to output port in Fig. 8. A comparison of simulated magnitudes and phases between the circuit diagram and unit cell with lossless materials is pictured in Fig. 9. The curves show a good agreement with small variances which result from neglected parasitic effects in the ECD. Consequently, the assumption is supported that the structure can be represented by the circuit model of fifth order in Fig. 8 and that its working principle agrees with a bandpass filter.

In summary, the FSS either can be considered as substrate filled resonator with multiple modes that are excited and loaded by two orthogonal slots or as bandpass filter that can be approximated by the introduced ECD.

B. Oblique Incidence

For the purpose of using the presented polarization rotator as reflective structure according to Fig. 1(b), an oblique incidence is required. Therefore, Floquet mode 1 is parallel ($\parallel$) and Floquet mode 2 is perpendicular ($\perp$) polarized with respect to the plane of incidence. In the following, Floquet mode 1 is excited for simulations and thus simulated S-parameters are named $S_{\parallel\parallel}$ and $S_{\perp\parallel}$. Referring to Fig. 3, when the angle of incidence ($\varphi = 0°, \theta > 0°$) is increased, a performance decrease can be observed in the S-parameters, as shown in Fig. 10. The polarization rotating effect is distorted and a reflection of the incident polarization occurring at approximately 15.40 GHz can be observed. This frequency matches the resonant frequency of mode 2 in Fig. 4, which is excited

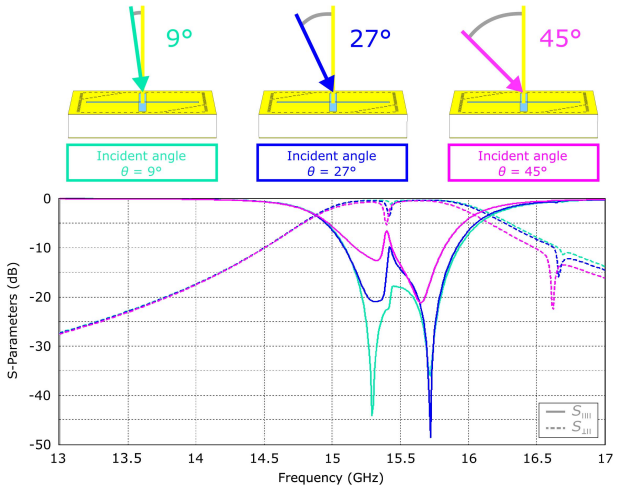

Fig. 10. Magnitude plots of S-parameters of Ku-band unit cell over frequency for incident angles $\theta = 9°$, $\theta = 27°$, and $\theta = 45°$.

due to component $\vec{E}_z$ of the incident wave defined in Fig. 3(b). In order to avoid this effect, mode 2 has to be suppressed without effecting the desired field distributions of modes 1 and 3 significantly in the SIW cavity. For this purpose, a single via with 0.40 mm diameter is added to the middle of the structure. Due to manufacturing constraints, a via restring with 0.80 mm diameter is added that must not short-circuit the slots. Following the boundary conditions of the Maxwell equations, electric field components must be perpendicular to electrically conductive surfaces. A via in the cavity center is oriented parallel to the E_z field component of mode 2 and consequently suppresses this undesirably excited mode. At this position, the z-components of modes 1 and 3 are zero and will not be affected by this via ideally. In fact, the resonance frequencies of those modes are shifted because the cavity dimensions are changed. For the evaluation of the suppression, an additional Eigenmode simulation is done, as pictured in Fig. 11. It can be observed that Mode 1′ and Mode 2′ in Fig. 11 correspond to Modes 1 and Mode 3 from Fig. 4. Unwanted mode 2 is no longer resonant and thus could be suppressed successfully.

After polarization rotation, the transmitting slot radiates in positive z-direction. However, if an array arrangement of multiple unit cells is established, each cell is excited with a phase shift due to oblique incidence. Consequently, transmitting slots are excited with the same phase shift resulting in the desired oblique emerging wave.

In contrast to a normal incidence, an oblique incident wave leads to a changed slot impedance due to changed field components referring to Fig. 3(b). Thus, the impedances of x-aligned receive and y-aligned transmit slots must be adjusted differently. The final and optimized simulation model with modified slot apertures is shown in Fig. 12. The corresponding S-parameters for the Ku-band unit cell appropriate for oblique incidence are depicted in Fig. 13. At 13.75 and 16.45 GHz, local perturbations can be seen which occur due to additional modes resonant in the cavity. In the polarization rotating band, a satisfying performance is achieved, while the performance of the polarization preserving band is still low due to finite

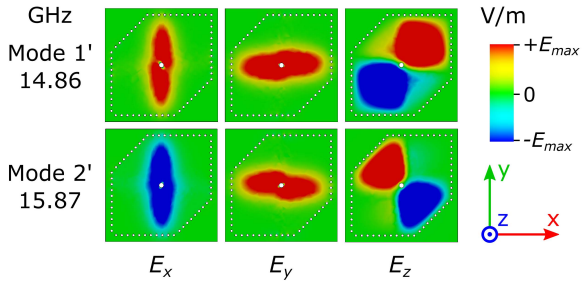

Fig. 11. Contour plots of electric field components in the SIW cavity with additional center via calculated with the Eigenmode solver. Fields are depicted in a cutting xy plane and amplitudes are linearly color-coded between $\pm E_{max}$.

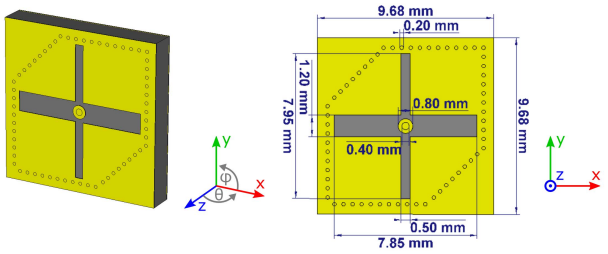

Fig. 12. CST model of Ku-band unit cell for oblique incidence ($\varphi = 0°$, $\theta = 45°$) from positive z-direction.

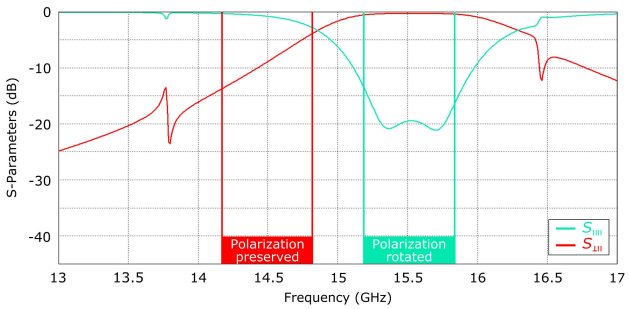

Fig. 13. Magnitude plots of S-parameters of Ku-band unit cell over frequency for oblique incidence ($\varphi = 0°, \theta = 45°$) from positive z-direction.

filter order of the design. Based on this unit cell, an FSS with 15×15 cells is assembled and manufactured.

IV. Ka-Band Reflector and Manufacturing Tolerances

In order to prove that the proposed concept of the SIW-based polarization rotating reflector is suitable for higher frequencies and to perform measurements on a 35 GHz SAR platform in the future, a Ka-band reflector is also developed. This reflector shall be usable for the frequencies in Table I and is designed with the experience gained from the Ku-band reflector. Increasing the frequency of operation leads to smaller unit cell dimensions and the sensitivity to manufacturing tolerances increases. Moreover, the diameter of the via placed in the center of the cavity needs to be smaller which cannot be realized by standard fabrication processes resulting in higher costs. To deal with these challenges, the substrate material is

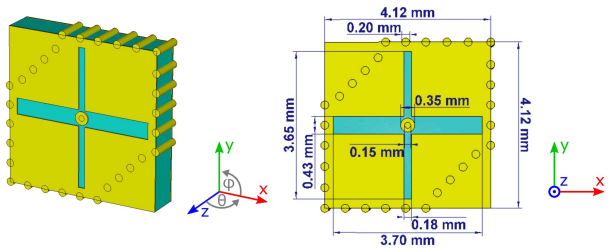

Fig. 14. CST model of Ka-band unit cell for oblique incidence ($\varphi = 0°$, $\theta = 45°$) from positive z-direction.

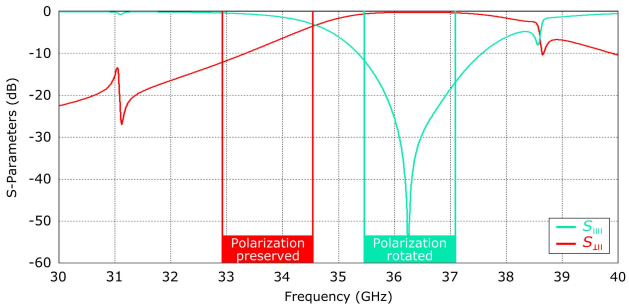

Fig. 15. Magnitude plots of S-parameters of Ka-band unit cell over frequency for oblique incidence ($\varphi = 0°, \theta = 45°$) from positive z-direction.

changed to Rogers RT5880 with reduced relative permittivity of $\varepsilon_r = 2.2$.

Slanted via edges are tuned by using the Eigenmode solver and slot impedances are optimized. Due to smaller slot dimensions, a 0.15 mm diameter via with 0.35 mm diameter restring is used, which can still be produced mechanically. The CST model with substrate thickness of 0.787 mm is depicted in Fig. 14. Due to changed substrate permittivity and thickness, impedances are changed and mode frequencies are shifted. As a result, the resonance coupling must be increased to achieve a performance compared with the Ku-band reflector. Simulated S-parameters of the optimized unit cell model are given in Fig. 15. Two perturbations at 31.10 and 38.60 GHz can be observed which are additional modes similar to the Ku-band design. Those modes are also slightly excited, but not disturbing the functionality due to out of band resonance.

Especially when using SIW structures for high-frequency applications, fabrication tolerances can have a significant influence on the system performance. In addition, the slot aperture is crucial and requires to be manufactured accurately. Before fabricating the Ku- and Ka-band reflectors, the effects of tolerances have been evaluated by applying a Monte Carlo method with randomly changing copper thickness, slot dimensions, and via positions on one unit cell. The assumed maximum deviation for copper thickness and via positions is ± 10 μm and for slot dimensions ± 15 μm. As the reflectors consist of multiple unit cells affected differently by manufacturing tolerances, the error in the frequency response of one unit cell can be considered as average error of an array arrangement. The tolerance investigations at Ku-band indicate frequency shifts of less than 100 MHz and matching differences of about 2 dB which can be assessed as negligible.

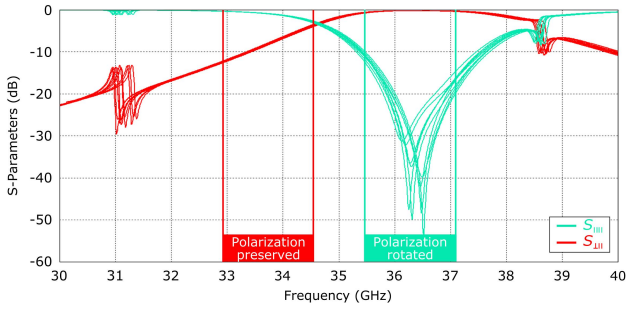

Fig. 16. Magnitude plots of S-parameters of Ka-band unit cell over frequency sensitivity analysis for oblique incidence ($\varphi = 0°, \theta = 45°$) from positive z-direction.

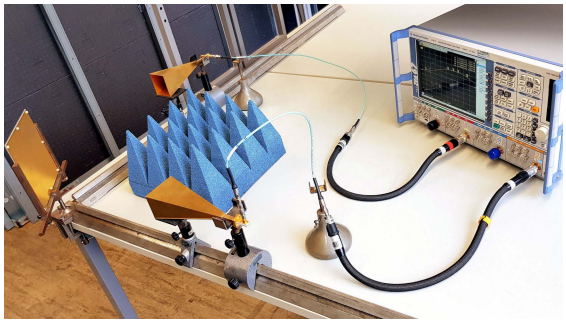

Fig. 17. Measurement setup with ZVA67 for Ka-band reflector.

The S-parameters of ten Monte Carlo simulations of the more sensitive Ka-band structure are presented in Fig. 16. It can be concluded that tolerances can lead to frequency shifts in the range of 250 MHz and matching degradations of about 3 dB at the band edges. However, the desired performance is still given for typical manufacturing tolerances.

V. Measurements

Several samples of the Ku-band and Ka-band reflector were fabricated. The reflectors consist of 15×15 unit cells and 45×45 unit cells with a size of 145×145 mm and 190×190 mm, respectively.

For evaluating the simulated S-parameters, the measurement setup shown in Fig. 17 is used. The FSS is mounted at a 45° angle at the intersection of two perpendicularly oriented metal profiles. Two linear polarized horn antennas are applied for the measurements, which are attached to the metal profiles with clamps. For Ku- and Ka-bands, different horn antennas are used. The distance between reflector and antenna is chosen in a way that the -11 dB width of the antenna diagram corresponds with the FSS boundaries. Applying an amplitude taper still excites all unit cells but reduces edge effects. Referring to reflector antenna theory, -11 dB edge illumination leads to the best compromise between aperture efficiency and spillover [15]. In order to attenuate direct crosstalk, absorber material is placed between the antennas. Hollow waveguide to 2.4 mm coaxial connector transitions is connected to both horn antennas to perform measurements with a Rohde&Schwarz ZVA67 vector network analyzer.

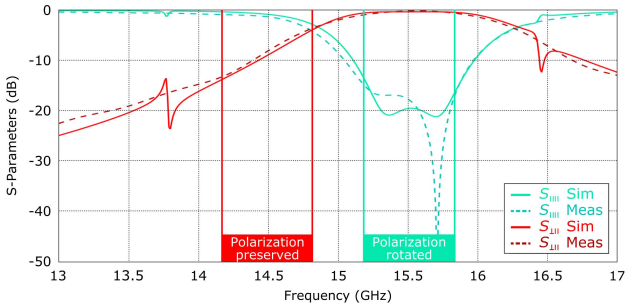

Fig. 18. Magnitude plots of measured and simulated S-parameters over frequency of the Ku-band reflector.

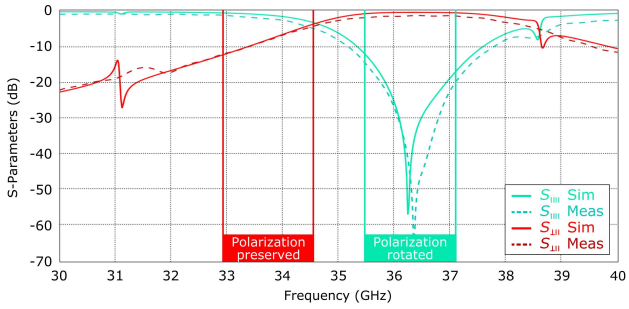

Fig. 19. Magnitude plots of measured and simulated S-parameters over frequency of the Ka-band reflector.

For calibration purposes, the reflector is exchanged by a metal plate and a through calibration is performed. This calibration method behaves as a normalization of the transmission factor S_{21} from port 1 to port 2 of the ZVA67. Due to mismatched system components like antennas, transitions, or coaxial adapters, multiple reflections occur in the measurement setup which cannot be eliminated with the used calibration method. Those multipath propagations lead to ripples in the S-parameters and can be observed in the time domain as additional peaks. Resulting from the applied calibration method, the reflector position is depicted in a range plot as a peak at 0 m distance. Applying a time gate from -0.4 to 0.4 m leads to a suppression of multiple reflections and thus eliminates the ripples from the S-parameter curves. Moreover, an averaging factor of 10 is used for noise reduction and dynamic clutter rejection.

VI. Discussion

Measurement results are depicted as dashed curves in Fig. 18 for Ku-band and Fig. 19 for Ka-band together with the simulation results taken from Figs. 13 and 15, respectively.

Referring to Fig. 18, it can be seen that a polarization preserving reflection is achieved in the lower frequency band and a polarization rotating reflection in the upper frequency band. It is noticeable that the lower resonance at 15.30 GHz is slightly detuned which indicates a deviation of the mode resonance coupling. However, the frequency shift is less than 50 MHz and, therefore, within the expected range resulting from fabrication tolerances. Out of band modes at 13.75 and 16.45 GHz mentioned in Section III are attenuated in the measurement data. This results from the applied time gating window function behaving as a smoothing filter and thus reducing the frequency domain resolution. Moreover, losses of 0.7 dB are higher compared with simulations. The comparison of simulation and measurement curves of the Ka-band reflector in Fig. 19 shows also a slight frequency and bandwidth deviation within the calculated tolerances depicted in Fig. 16. In contrast to Ku-band, local perturbations are visible in Fig. 19 at 31.10 and 38.60 GHz but less pronounced. This shows that out of band modes are present but attenuated due to time gating. Losses of around 0.9 dB occur in the polarization rotating band which are higher compared with the simulation.

Through an optical inspection with a microscope, it has been found that fabrication variations of copper structures and positions amount ± 20 μm and sharp edges of the rectangular slots are curved with 60 μm radius. As the Ka-band reflector is fabricated on a thinner substrate material, it shows a slightly bent surface.

An overall comparison of simulation and measurement results shows a very good agreement more than sufficient for a proof of concept. Deviations resulting from manufacturing tolerances and necessary calibration or signal processing are within expectations. Further investigations on measurement setup errors, e.g., polarization mismatch, neglected tolerances like the bent surface of the FSS or on dielectric losses still have to be carried out in detail. In order to avoid a bend reflector surface, an additional FR4 layer can be used for stabilization.

VII. Conclusion

A frequency-dependent polarization rotating reflector for polarimetric radar applications in Ku-band was designed and analyzed. The proposed system design exploits SIW-based cavities with rectangular crossed slots and chamfered cavity edges to rotate the polarization direction of a reflected linear polarized wave by 90°. An analysis of resonant modes within the cavity was performed and excited modes for different oblique incident angles were analyzed and—if necessary—suppressed by an additional plated through via hole in the cavity middle. Besides a resonator model, an ECD with a fifth-order filter was presented for describing the bandpass filter behavior of the unit cell. Good agreement between magnitudes and phases of S-parameters between ECD and unit cell simulations were achieved. Due to the limited filter order of the introduced structure, the performance in the polarization preserving reflection band is low in terms of polarization decoupling. The polarization rotation works satisfactorily with a decoupling of at least 13 dB. Furthermore, the reflector design has been adapted to the Ka-band. Ku- and Ka-band reflectors have been fabricated and their reflection properties have been determined by measurements for verifying the simulation results. The effects of fabrication tolerances have been investigated using a Monte Carlo approach. Measurements show good agreement with simulations; nevertheless, variations can be explained by manufacturing tolerances and signal processing within the expected range. In order to test the use of the described reflector for radar applications, the reflector shall be combined with an SAR system for expanding it to a polarimetric SAR system. Further developments could deal with improvements of cross polarization attenuation in

the lower band, e.g., by applying a multilayer structure with additional resonators. In the future, alternative concepts apart from the one presented here, e.g., transmissive FSS, electronically switched dipoles or mechanical polarization modification, could be investigated.

REFERENCES

[1] J.-S. Lee and E. Pottier, "Overview of polarimetric radar imaging," in *Polarimetric Radar Imaging: From Basics to Applications*. Boca Raton, FL, USA: CRC Press, 2009.

[2] T. Otto, H. W. J. Russchenberg, and H. Leijnse, "Advances in polarimetric X-band weather radar," presented at the 9th Eur. Radar Conf., Oct./Nov. 2, 2012.

[3] M. Jafari, Y. Maghsoudi, and M. J. V. Zoej, "A new method for land cover characterization and classification of polarimetric SAR data using polarimetric signatures," *IEEE J. Sel. Topics Appl. Earth Observ. Remote Sens.*, vol. 8, no. 7, pp. 3595–3607, Jul. 2015.

[4] C. López-Martínez, A. Alonso, X. Fàbregas, and K. P. Papathannassiou, "Ground topography estimation over forests considering polarimetric SAR interferometry," presented at the IEEE Int. Geosci. Remote Sens. Symp., Jul. 30, 2010.

[5] H. Wakabayashi, T. Matsuoka, K. Nakamura, and F. Nishio, "Polarimetric characteristics of sea ice in the sea of okhotsk observed by airborne L-band SAR," *IEEE Trans. Geosci. Remote Sens.*, vol. 42, no. 11, pp. 2412–2425, Nov. 2004.

[6] V. Akbari and C. Brekke, "Iceberg detection in open water and sea ice using C-band radar polarimetry," presented at the IEEE Int. Geosci. Remote Sens. Symp., Jul. 28, 2017.

[7] T. Vissentin, J. Hasch, and T. Zwick, "Polarimetric RCS measurements of selected two-wheeled vehicles for automotive radar," presented at the 14th Eur. Radar Conf., Oct. 13, 2017.

[8] H. Iqbal, C. Knill, M. Z. Khan, T. Chaloun, and C. Waldschm, "Polarimetric SAR for automotive applications," presented at the 15th Eur. Radar Conf., Sep. 28, 2018.

[9] H. Zhou, W. Hong, L. Tian, and M. Jiang, "A polarization-rotating SIW reflective surface with two sharp band edges," *IEEE Antennas Wireless Propag. Lett.*, vol. 15, pp. 130–134, 2016.

[10] M. S. M. Mollaei, "Narrowband configurable polarization rotator using frequency selective surface based on circular substrate-integrated waveguide cavity," *IEEE Antennas Wireless Propag. Lett.*, vol. 16, pp. 1923–1926, 2017.

[11] S. A. Winkler, W. Hong, M. Bozzi, and K. Wu, "Polarization rotating frequency selective surface based on substrate integrated waveguide technology," *IEEE Trans. Antennas Propag.*, vol. 58, no. 4, pp. 1202–1213, Apr. 2010.

[12] X.-C. Zhu *et al.*, "Design of a bandwidth-enhanced polarization rotating frequency selective surface," *IEEE Trans. Antennas Propag.*, vol. 62, no. 2, pp. 940–944, Feb. 2014.

[13] M. Saikia, S. Ghosh, and K. V. Srivastava, "Design and analysis of ultrathin polarization rotating frequency selective surface using V-shaped slots," *IEEE Antennas Wireless Propag. Lett.*, vol. 16, pp. 2022–2025, 2017.

[14] T. Dallmann, S. Stanko, and T. Bertuch, "Verfahren zur radarpolarimetrie sowie polarimetrisches radarsystem," German Patent 10/2017 220 734 A1, Nov. 21, 2017.

[15] C. A. Balanis, *Antenna Theory—Analysis and Design*, 4th ed. Hoboken, NJ, USA: Wiley, 2016, pp. 680–684, 830–832, 348–354, and 875–923.

[16] R. F. Harrington, *Time-Harmonic Electromagnetic Fields*. New York, NY, USA: McGraw-Hill, 1961.

[17] D. M. Pozer, *Microwave Engineering*, 3th ed. Hoboken, NJ, USA: Wiley, 2005, pp. 337–345.

Tim Freialdenhoven was born in Simmerath, Germany, in 1990. He received the M.Sc. RWTH degree in electrical engineering, information technology, and computer engineering from RWTH Aachen University, Aachen, Germany, in 2015. He is currently pursuing the Ph.D. degree in electrical engineering with the Research Group Aachen, Fraunhofer FHR, Aachen.

From 2015 to 2017, he worked as a Microwave Design Engineer with indurad GmbH, Aachen. Since 2017, he has been a part of the Research Group Aachen, Fraunhofer FHR. His research is focused on microwave circuit and antenna design specialized for radar systems.

Thomas Bertuch (Member, IEEE) received the Ph.D. (Doktor der Ingenieur-wissenschaften) degree from RWTH Aachen University, Aachen, Germany, in 2003.

His doctoral research was developed at the Research Institute for High Frequency Physics and Radar Techniques of the Research Establishment for Applied Natural Science e.V. (FGAN-FHR), Wachtberg, Germany. In 2004, he was a Senior Antenna Scientist with the Defence, Security and Safety Institute, The Netherlands Organization for Applied Scientific Research (TNO), The Hague, The Netherlands. Since 2005, he has been with the Fraunhofer Institute for High Frequency Physics and Radar Techniques (FHR) (formerly FGAN-FHR), Wachtberg, where he is currently a Team Leader of antennas and front-end technology. His main research activities are antenna and microwave circuit design, engineered electromagnetic materials (metamaterials), electromagnetic modeling, and RF heating.

Stephan Stanko received the Diploma degree in physics and the Dr.rer.-nat. degree from Cologne University, Cologne, Germany, in 1998 and 2002, respectively.

From 2002 to 2005, he was a Post-Doctoral Researcher with the University of Bonn, Bonn, Germany. In 2005, he joined Fraunhofer FHR (formerly FGAN-FHR), Wachtberg, Germany. His research interests include high-frequency radar systems, especially millimeter- and submillimeter-wave imaging radar systems, system miniaturization, small flying platforms, digital back ends, and radiometry.

Denis Nötel was born in Hildesheim, Germany, in 1976. He received the Dipl.-Ing. degree from Technische Universität Braunschweig, Braunschweig, Germany, in 2004.

Since then, he has been a Research Staff Member with the Fraunhofer Institute for High Frequency Physics and Radar Techniques (FHR), Wachtberg, Germany. His research interests include radar and radiometry in the millimeter-wave regime.

Diana I. L. Vorst received the B.Eng. degree in electrical engineering from the University of Applied Sciences Bonn-Rhein-Sieg, Sankt Augustin, Germany, in 2017.

Since 2014, she has been a part of the High Frequency Radar and Application Department, Fraunhofer Institute for High Frequency Physics and Radar Techniques (FHR), Wachtberg, Germany, where her focus is on RF measurements of all kinds as well as the associated equipment and measurement methods.

Thomas Dallmann (Member, IEEE) was born in Aachen, Germany, in 1985. He received the Dipl.-Ing. degree in electrical engineering from RWTH Aachen University, Aachen, in 2010, and the Ph.D. degree from the Institute of High Frequency Technology IHF, RWTH Aachen University, in 2017. His thesis was on polarimetric radar cross-section imaging.

From 2009 to 2010, he was with Rohde & Schwarz, Munich, Germany. From 2010 to 2016, he worked as a Research Assistant with the Institute of High Frequency Technology IHF, RWTH Aachen University. Since 2016, he has been leading the Research Group Aachen, Fraunhofer-Institute for High Frequency Physics and Radar Techniques (FHR), Aachen, where he is involved in the development of new sensor concepts and validation approaches for automotive radar.